Inertial Flow Structures in a Simple-Packed Bed of Spheres

Tetsuya Suekane, Yasuo Yokouchi, and Shuichiro Hirai
Research Center for Carbon Recycling and Energy, Tokyo Institute of Technology, Tokyo, 152-8552 Japan

The detailed characteristics of the interstitial velocity distributions in pores are critical to understanding heat and mass transfer in a packed bed of granular material. The velocity distributions in a pore that models a simple-packed bed were measured directly by a magnetic resonance imaging technique. With an increase in the Reynolds number from 12.17 to 59.78 − 204.74, the increase and decrease in main flow velocity did not correspond to the local pore geometry, as is the case with a creeping flow. This indicated that inertial forces dominate over viscous forces. For example, at the Reynolds number of 204.74, the fluid penetrated through the center of the pores like a jet with negligible change of velocity. Circulation in the surrounding stagnant spaces generated eight symmetrical eddies in the plane perpendicular to the main flow direction.

Introduction

The physical understanding of fluid flow in a packed bed of granular material is essential for many science and engineering applications. Investigation of these phenomena has applications to various chemical and mechanical engineering systems including heat and mass transport in a packed bed, oil recovery from rock formations, packed-bed-reactor design, and filtration systems. For Reynolds numbers Re below about unity, the pressure drop per unit length along the main flow direction in porous systems varies linearly with the filtration velocity in accordance with Darcy's law; whereas, as velocity increases, deviations from Darcy's law occur due to the inertial contribution to the momentum balance (Bear, 1972; Kaviany, 1995). Heat and mass transfer in a packed bed are sensitive to the details of the interstitial velocity distributions in pores over a wide range of Reynolds numbers.

Attempts have been made in the past to clarify the flow structure in packed beds at the Reynolds numbers for the transition from laminar to turbulent flow. Jolls and Hanratty (1966) studied the motion of a colored plume of fluid through a packed bed of spherical particles. A transition from laminar to turbulent flow occurred over the Reynolds number range 268 to 366. Dybbs and Edwards (1984) used laser anemometry to visualize the flow of liquids in porous structures built out of spheres in a hexagonal packing and also rods arranged in a complex, fixed, three-dimensional (3-D) geometry. There were four flow regimes as a function of Reynolds number: (1) Darcy or creeping flow at $Re < 1$; (2) inertial flow at $1 < Re < 150$; (3) unsteady, laminar flow at $150 < Re < 300$; and (4) highly unsteady flow at $Re > 300$.

Various improvements in measurement technique have allowed the detailed investigation of flow in porous media. Among these are laser-Doppler anemometer (LDA) (Yevseyev et al., 1991), particle image velocimetry (PIV) (Stephenson and Stewart, 1986; Saleh et al., 1993; Rashidi et al., 1996; Moroni and Cushman, 2001), photoluminescent volumetric imaging (PVI) (Montemagno and Gray, 1995), magnetic resonance imaging (MRI) (Shattuck et al., 1991, 1995; Li et al., 1994; Kutsovsky et al., 1996; Seymour and Callaghan, 1997; Sederman et al., 1997, 1998; Manz et al., 1999; Irwin et al., 2000), and magnetic resonance tomography (MRT) (Baumann et al., 2000). Reviews of the MRI work on porous media are in Bories et al. (1991) and Fukushima (1999). For measurements of flow in porous media, optical techniques such as LDA and PIV can be applied to only solid and liquid phases of the same refractive index, whereas MRI requires that the porous media be nonmagnetic. In the present study, MRI was used to visualize directly the flow field in porous media.

MRI techniques have shown structure-flow correlations within the inter-particle space of randomly packed beds of spheres (Sederman et al., 1998; Johns et al., 2000). In particular, Sederman et al. (1998) observed significant heterogeneity in the flow; for example, approximately 8% of the pores carry

Correspondence concerning this article should be addressed to T. Suekane.

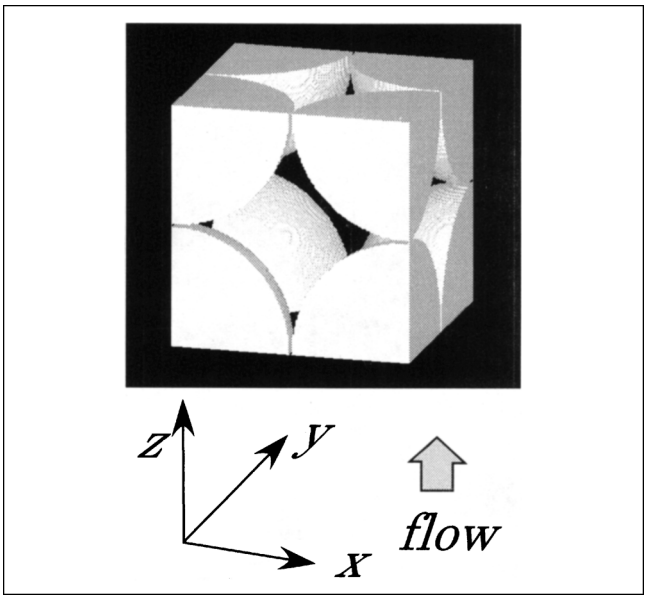

Figure 1. Unit cell for a bed of uniform spheres in a simple cubic lattice.

Origin of the coordinates is in the center. The image was constructed from the MRI data obtained in present experiments.

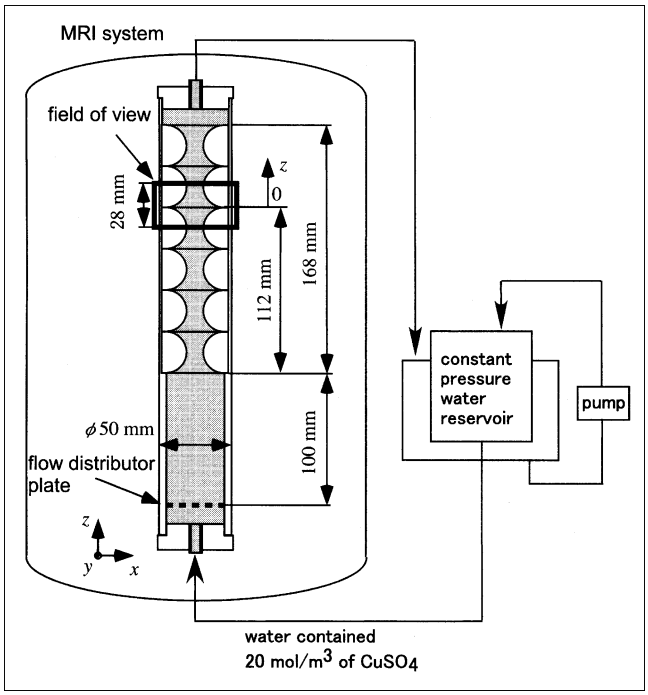

Figure 2. Experimental apparatus.

Measurements were done in the region near the top of the channel and marked by the rectangle marked as 28 mm high.

40% of the volume flow, and high volume flow is mostly influenced by the local geometry of the pore space. Ogawa et al. (2000) used MRI analysis to show that most of the channel flows with higher axial velocity are induced in the axial channels with long, straight pores. Johns et al. (2000) extended the study by Sederman et al. to investigate in detail the transition from creeping to inertial flow in a randomly packed bed. They found that the transition was sensitive to the local Reynolds number of each pore and the nearly-stagnant fluid had a large influence on the pressure distribution. However, it is still not clear how each separate factor, pore heterogeneity and intrinsic flow instability, influences the flow within randomly packed beds.

This article describes our measurements of flow velocities in a simply packed bed of spheres in the range of Reynolds number from the inertial flow region to the transition to the unsteady laminar flow region. In the simply packed bed, spheres are arranged at each corner of the cube, as shown in Figure 1. The unit cell had simple cubic packing with an average volumetric porosity ϵ of 0.476. Taking into account the flow symmetry, we modeled the flow in a packed bed by focusing on the flow through six unit cells along one flow channel. Because there is no net flow and pressure gradient across symmetry plates in x- and y-directions, the symmetry plates were replaced by a solid wall as in Figure 2. The three components of the velocity vectors of the fluid in 3-D pore space of the channel were directly measured using an MRI technique with high resolution. Velocity distributions in the pore are shown for Reynolds numbers over the transition from Darcy to inertial flows.

Experimental Apparatus and Measurement Techniques

Figure 2 shows the apparatus, which consisted of the flow channel aligned vertically inside the MRI system and a water circulating system with a constant-pressure water reservoir. The channel models an ideal series of five unit cells, hereafter unit pores, in a simply packed bed. Each pore is bound by two layers, as shown in Figure 2; thus, we used six plastic unit layers arranged in an acrylic pipe. The layers were 28 mm on each side and were put in a cylinder 46 mm in diameter. Each of the six layers had four 1/4-spheres of 28 mm diameter D_p, as shown in Figure 3. The layers were aligned in the pipe by putting tubes through the holes on each side. During the experiments, stationary water contained in these tubes was used as a velocity reference. A flow distributor plate was 100 mm upstream from the entrance of the unit cell channel to make the flow uniform, as shown in Figure 2. Water was circulated from the reservoir with a constant pressure to keep the flow rate constant. Measurements of the flow rate were repeated several times during the course of an experiment to ensure that the flow rate Q was constant. We averaged the measured velocities in the fourth unit pore downstream (that is, between the fourth and fifth layers shown in Figure 2), because our preliminary experimental results showed that the velocity field is periodic by the time the water reaches this pore. The averaging was done to reduce fluctuations that might result from distortion of applied magnetic field and the velocity fluctuations. The point between these two layers on the axis of the channel is the origin of x, y, z coordinates with the z axis pointing downstream.

Our MRI system (Varian model Unity Inova 300/150 SWB) imaged the spatial distribution of the flowing water by receiving the signals from protons rotating with their Larmor frequency, which is proportional to the intensity of the applied magnetic field. The strength of the magnetic field of this system was 7.05 T, and the bore diameter was 57 mm. Gradient

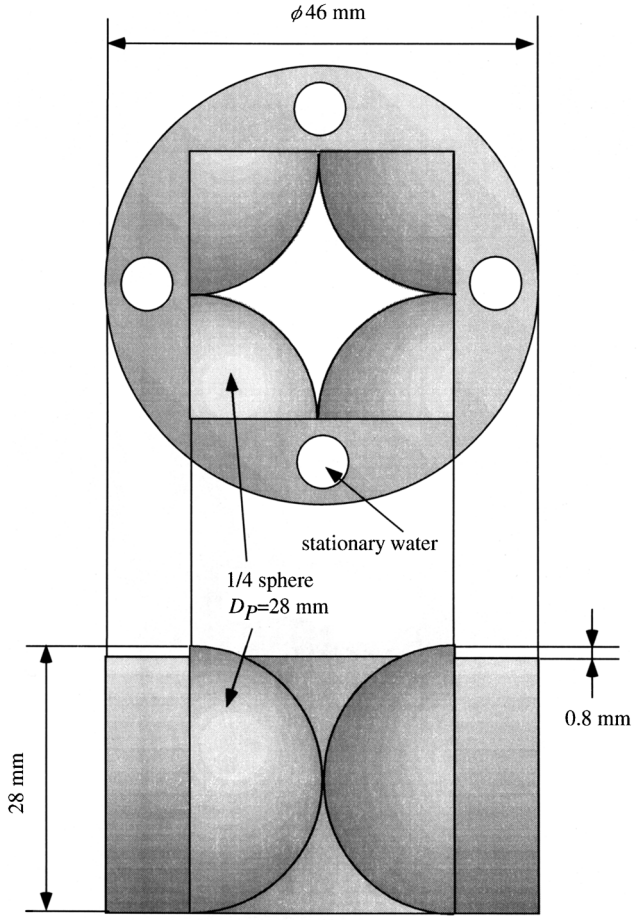

Figure 3. Top and side view of the unit cell.

Clearance on top surface of the cell is for the rubber packing to prevent water leakage. Unit cells were made of acrylonitride-butadiene styrene.

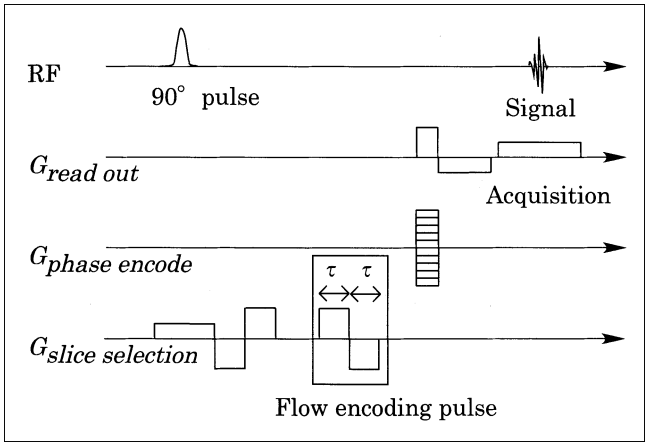

Figure 4. Phase encoding method for flow measurement.

$G_{read\ out}$, $G_{phase\ encode}$ and $G_{slice\ selection}$ correspond to the magnetic field gradient in x-, y- and z-directions, respectively. The duration of flow encoding pulse τ is 0.0025 s.

coils provided a maximum gradient strength of 0.24 T/m. Further details of MRI techniques for fluid flow can be found in Callaghan (1991) and Fukushima (1999).

Velocity distributions were measured using the phase encoding method, which is a technique used to acquire the velocity distribution in a cross section (Feinauer et al., 1997). A timing diagram of the radio frequency and magnetic field gradient pulses for obtaining an image of the fluid velocity distribution is shown in Figure 4. A flow encoding pulse is included in the pulse sequence of conventional gradient echo imaging. Under a magnetic field gradient of magnitude G imposed for flow encoding, the velocity is related to the phase of the Larmor precession generated by the difference in Larmor frequency that corresponds to the position of the proton. The proton's $\Delta\Phi$ is

$$\Delta\Phi = \gamma G v_0 \tau^2 \tag{1}$$

where γ is the gyromagnetic ratio of the proton, v_0 is the component of the flow velocity along the flow encoding gradient, and τ is the duration of the imposed flow encoding gradient. In the present study, $\Delta\Phi$ is the phase difference between the phase measured with flowing water and with stationary water. The measurement accuracy in this method is 15% for a well developed Hagen-Poiseuille flow in a cylindrical tube with the spatial resolution of 0.2 mm $\times$ 0.2 mm $\times$ 0.5 mm (Ogawa et al., 2000). Images of the pore structure were acquired simultaneously with the phase difference to determine the velocity v for each pixel.

For the velocity experiments, the field of view is 51.2 mm $\times$ 51.2 mm in the x-y plane, and the thickness of a slice along the direction of main flow is 0.5 mm. The spatial resolution was 0.2 mm $\times$ 0.2 mm. For each plane, each of three velocity components is the average of three measurements. At equal space intervals of about 2.0 mm in the main flow direction, 17 planes of velocity distribution were obtained over the 28 mm field of view shown in Figure 2; hence, the velocity distribution was obtained in the entire unit cell pore space of Figure 1. To reduce the spin-lattice relaxation time of water and thus decrease the image acquisition time, the water contained 20 mol/m^3 of copper sulfate.

The Reynolds number is defined here as

$$Re = \rho v_{\text{mean}} D_p/\mu, \tag{2}$$

$$v_{\text{mean}} = Q/A\epsilon, \tag{3}$$

where ρ and μ are the fluid density and viscosity of fluid, D_p is the diameter of the packed spheres, v_{mean} is the average downstream (z) component of the water flow velocity, and $A = D_p^2$, the cross-sectional area of the packed bed. The Cartesian coordinates are normalized by the sphere radius $r = D_p/2$ and hence vary between -1 and 1.

Experimental conditions are summarized in Table 1. Three velocity components were visualized in detail at the Reynolds number of 12.17, 59.78, and 204.74. The lower two Reynolds numbers correspond to the inertial flow region, and the highest corresponds to the unsteady laminar flow region. At $Re =$ 12.17, the flow is in transition from creeping to inertial flows, whereas at $Re =$ 204.74, the flow is in transition from inertial to unsteady laminar flows. Because the fluctuation time scale

Table 1. Experimental Conditions*

Re	*Q* [mm³/s]	v_{mean} [mm/s]
12.17	162.21	0.435
28.88	384.90	1.031
59.78	796.77	2.135
105.57	1,407.0	3.770
204.74	2,728.7	7.312

*Re is the Reynolds number, Q is the flow rate; v_{mean} is the pore-averaged value of v_z.

is about 1 s and, hence, much shorter than the image acquisition time of about 140 s, measured velocities are time averages over many fluctuations. At the slice $z = 0$, v_z was also measured at supplemental Reynolds numbers of 28.88 and 105.57.

Experimental Results and Discussion

Velocity distributions are shown in Figure 5 for the lowest, middle, and highest *Re*. Because of the symmetry of the flow in the *x*- and *y*-directions, only one quadrant in *x*-*y* space is shown. The magnitudes of the velocities v are normalized by the average pore velocity v_{mean}. At the lowest Reynolds number of 12.17, the water moves along the sphere surfaces and, thus, the velocities decrease with an increasing cross-sectional area normal to the main flow. In other words, only the cross-sectional area of local pore affects the velocity distribution. Therefore, the distribution of velocities has the symmetry of the pore structure. These properties are typical of a creeping flow, although, at this Reynolds number, the relation between the pressure drop and the fluid velocity deviates from Darcy's law. At $Re = 204.74$, the velocity does not depend on the cross-sectional area; the fluid penetrates through the pore space like a jet without changing velocity. At the intermediate Reynolds number of 59.78, the velocity along the flow direction does not simply decrease as the cross-sectional area increases, and then increases as the cross-sectional area decreases further downstream. Instead, the downstream flow speed has a minimum downstream from the maximum in cross-sectional area. At this intermediate *Re*, the inertial forces dominate over viscous forces; the water is flowing so fast that it flows past the maximum cross section before it slows down.

If the velocity components in the z-direction v_z are integrated over the cross-sectional area, the result at every slice should be constant and equal to the flow rate Q measured at the exit of the water circulation loop. This serves as a check of our data analysis. The v_z integrated over each slice, and then averaged over all 17 slices in the pore, are within 8% of Q for $Re = 12.17$, 59.78, and 204.74 (Figure 6). This is consistent with the estimated 15% measurement accuracy of lo-

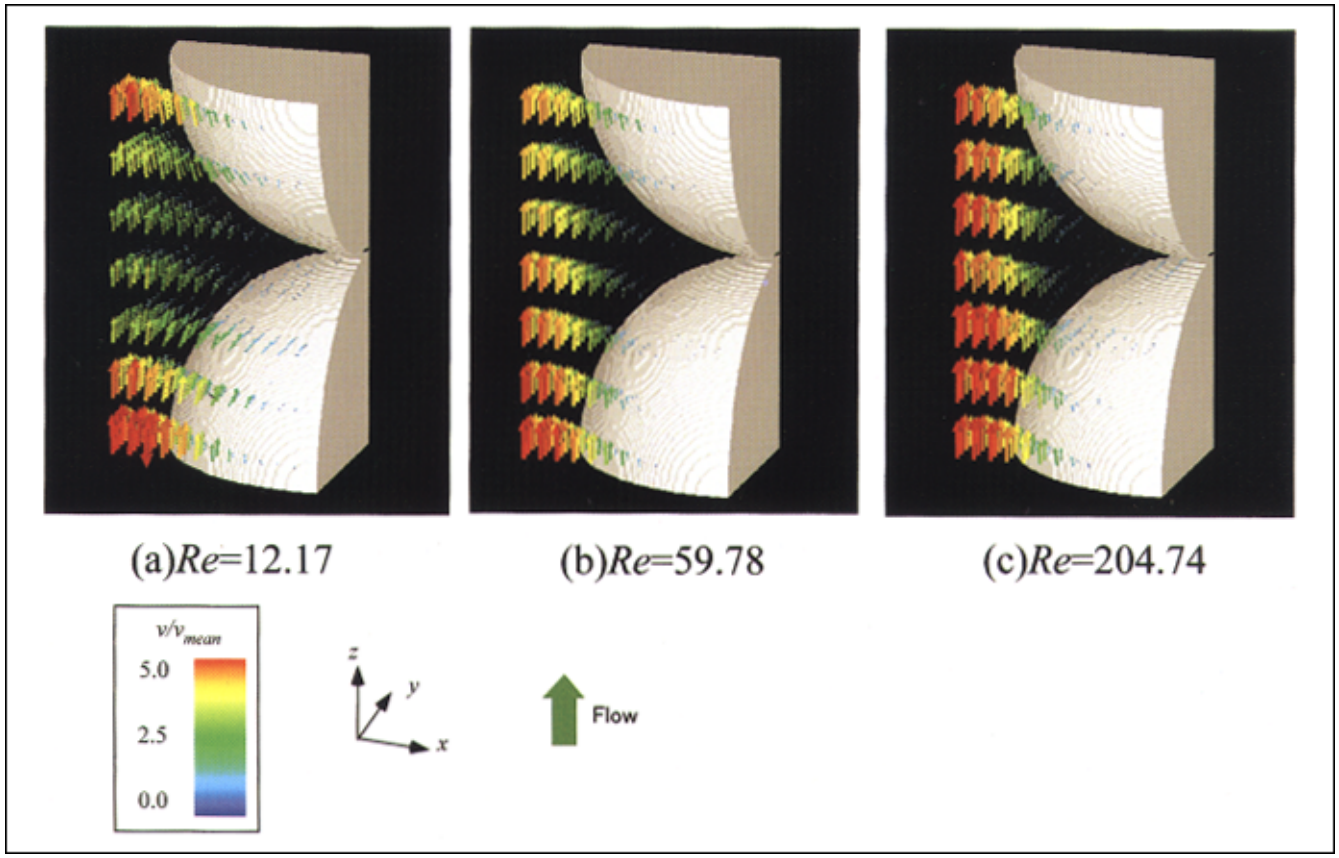

Figure 5. Velocity distributions in a quarter pore for the three Reynolds numbers shown below each plot.

(a) $Re = 12.17$, (b) $Re = 59.78$, and (c) $Re = 204.74$. Arrows are colored according to the magnitude of local velocity normalized by the averaged pore velocity v/v_{mean}.

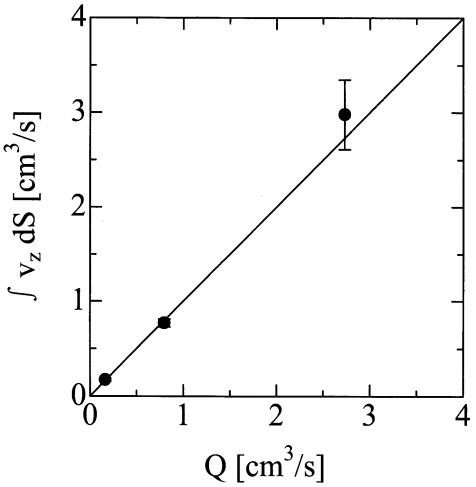

Figure 6. Relation between volumetric flow rate obtained from the axial velocity images and flow rate measured at the exit of the water circulation loop *Q*.

Solid line represents perfect correlation. The total flow rate calculated for each slice was averaged over all 17 slices.

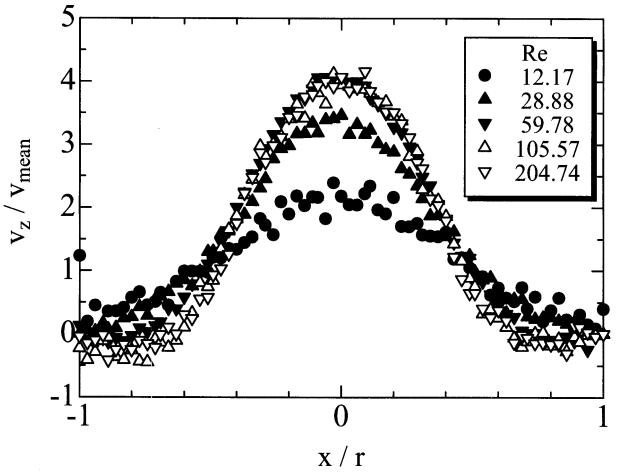

Figure 7. Effect of the Reynolds number on the velocity distribution along the *x*-axis at the highest cross-sectional area $z = 0$ and $y = 0$.

Walls are at $x = -1$ and $+1$. Because of the distortion of the applied magnetic field near the walls, the imaged velocities are nonzero at the walls.

cal velocity for a well-developed Hagen-Poiseuille flow in a cylindrical tube. The complicated structure of the packed bed might distort here the distribution of magnetic flux density near the spheres' surfaces in spite of their material being nonmagnetic. Velocity fluctuations during the data acquisition time also affect measurement accuracy. However, a more precise estimate of accuracy is very difficult.

Along the $z = 0$, $y = 0$ line, the z-component of the velocity peaks at the center of the pore, and this peak is sharper at the larger Reynolds numbers (Figure 7). If the velocity was uniform in the slice perpendicular to the main flow direction, mass conservation would require that v_z/v_{mean} equal 0.476 and 2.214 for the largest and the smallest cross-sectional areas, respectively. However, the velocity is not uniform across a slice. For example, at $Re = 12.17$, the maximum $v_z/v_{\text{mean}} \sim 2$ instead of 0.476. The velocity decreases to zero gradually at the walls (that is, $x/r = \pm 1$). The velocity profiles are symmetrical to the plane $x = 0$ up to $Re = 204.74$. The value of maximum v_z increases with Reynolds number up to the value of 4 v_{mean} and tends to be constant in the range of Reynolds number from 59.78 to 204.74. Reverse flow arises at the points near the wall at high Reynolds numbers, and, thus, most of the volumetric flow is in the center of the pore. Within a single pore space of a randomly packed bed, the high velocity region has a parabolic profile that coexists with the surrounding near-stagnant region.

Axial velocity images in five slices in the main flow direction at $Re = 12.17$, 59.78, and 204.74 are shown in Figure 8. Slice C ($z/r = 0.0$) contains no spherical surfaces of the channel; the square slice area is filled with water. In slices B ($z/r = -0.28$) and D ($z/r = 0.28$), the four spheres show up as four quarter-circles, one at each corner, with normalized radii of 0.694. Similarly, slices A and E have circles with normalized radii of 0.898 at the corners (Figure 8). As shown also in Figures 5 and 7, at low Re, the velocity generally decreases with increasing cross-sectional area and increases with decreasing cross-sectional area along the main flow line. At $Re = 59.78$, extensive reverse flow occurs near the surfaces of the spheres in the slices A-C; in this sequence, the cross-sectional area increases along the main flow direction. The inertial forces are significant at this Reynolds number. At $Re = 204.74$, the fluid flows through the center of the pore with negligible change in velocity. For all Reynolds numbers, the velocity distribution is nearly symmetrical in x and y in every slice.

Figure 9 shows the normalized variance of the velocity distribution in slices perpendicular to the main flow direction versus the local Reynolds number Re_l. The normalized variance is defined by the variance of the z-component of velocity σ divided by the average velocity $\bar{v}_z$. A local Reynolds number is defined in Sederman et al. (1998) and Johns et al. (2000) as

$$Re_l = \frac{d\rho\bar{v}_z}{\mu} \tag{4}$$

where d is the distance between spheres along the line $x = y$ in Figure 8 and $\bar{v}_z$ is the average velocity in the slice, as calculated from the experimental data. For all three Reynolds numbers, the normalized variance decreases with an increase in the local Reynolds number. However, the decrease of the normalized variance does not result from a flattening of the velocity profile such as that for a randomly packed bed (Johns et al., 2000). The velocity distribution of the jet-like flow that penetrates the pore center is parabolic (Figure 8). The change in the normalized variance results from the ratio of the surrounding near-stagnant region's area to the jet-like flow area. The flattening of the velocity distribution, which resembles a laminar flow at the entrance to a pipe, might result from the winding of the streamlines due to the tortuosity of a randomly packed bed. In a simply packed bed, the velocity distribution of the jet-like flow remains parabolic because it pene-

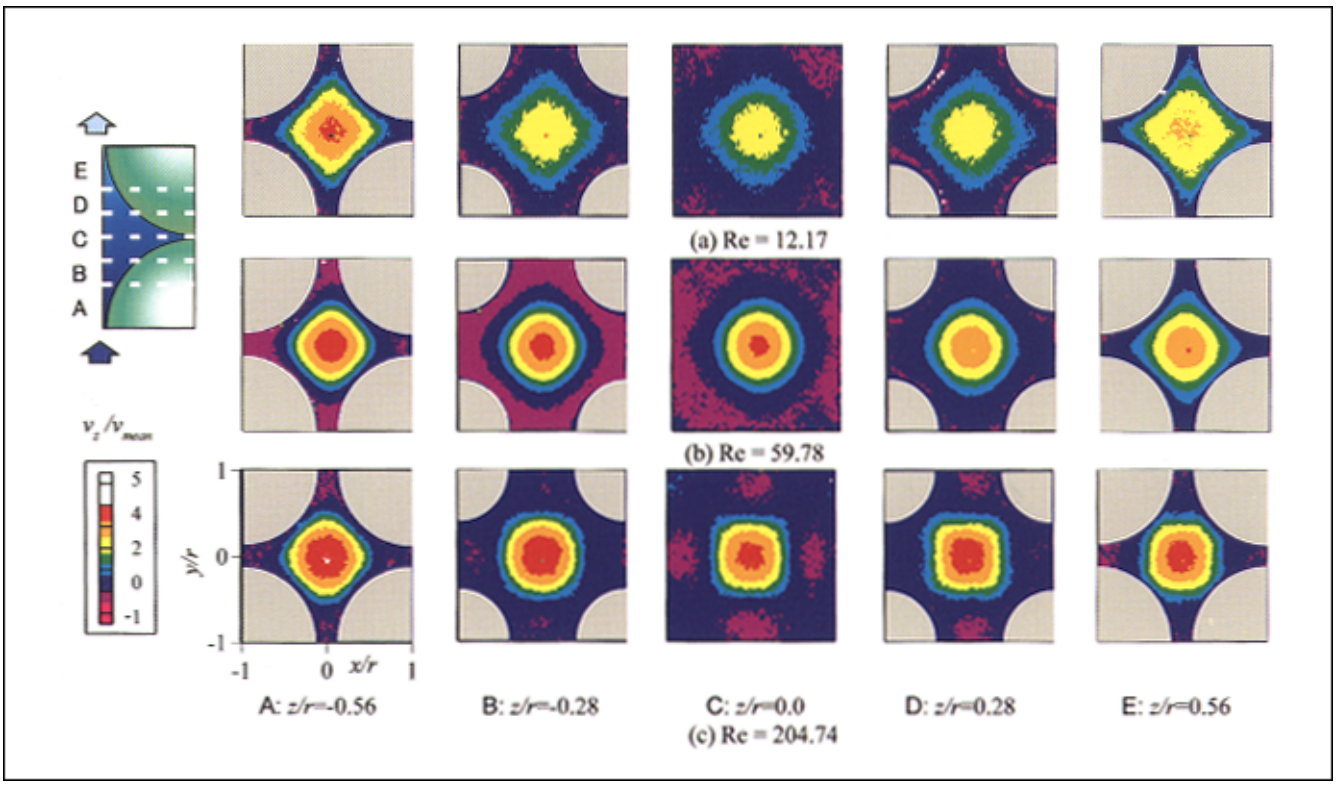

Figure 8. Axial velocity images in five 0.5 mm thick slices at the Reynolds number of (a) 12.17, (b) 59.78, and (c) 204.74.

Slices are located at equal space intervals in the main flow direction as indicated by dashed, white lines in the drawing at left and listed along the bottom of the images. Measured axial velocities v_z are normalized by the averaged pore velocity v_{mean}.

trates through the pores without changing direction. Moreover, within a randomly packed bed, the local Reynolds number varies over a wide range, even for relatively low bulk Reynolds numbers, because of the redistribution and concentration of flow. However, in the present experiment, because of mass conservation, the local Reynolds number is inversely proportional to the cross-sectional area. Therefore, the concept of the local Reynolds number cannot be directly applied to describe the velocity distribution within a simply packed bed. The velocity distribution within the pore of a simply packed bed is different from that of a randomly packed bed.

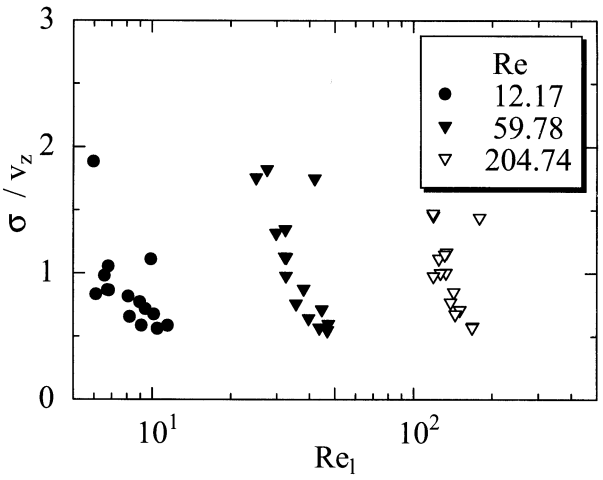

Figure 9. Relation between the local Reynolds number Re_l and the normalized variance of velocity in a plane perpendicular to the main flow direction.

Figure 10 shows horizontal flow patterns in three downstream slices A, B, and C that have sequentially-decreasing cross-sectional areas along the main flow direction. Because the flow fields are symmetrical in x and y, Figure 10 shows only one quadrant of the pore space. The flow fields are also nearly symmetrical to the line $x = y$. For the creeping flow (not shown), the fluid moves in the direction from the right top corner to the left bottom to avoid the sphere. Conversely, at $Re = 59.78$ and 204.74, the flow collides on the sphere surface and turns towards the stagnant spaces near the left top and right bottom corners. At $Re = 59.78$, the flow moves away from the surface of the sphere in the slice $z/r = 0.42$. At $Re = 204.74$, two eddies arise clearly in the slice $z/r = 0.14$. For both Reynolds numbers, the magnitudes of the velocity components in the x-y plane v_x, v_y are much lower than that of v_z at the center of the pore (relative size is shown at left). Thus, the motion of fluid in the x- and y-directions are practically negligible except in the near-stagnant region where v_z is comparable to v_x and v_y.

Figure 11 shows the 3-D structure of the flow at $Re = 204.74$. The initial points for these streamlines in the x-y plane are shown in the drawing at the left; the three central ones

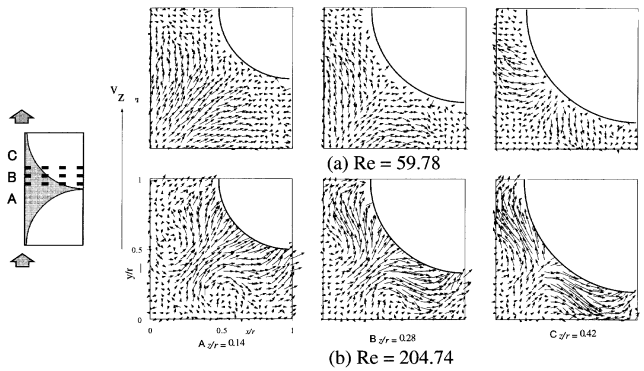

Figure 10. Horizontal flow at (a) *Re* = 59.78 and (b) *Re* = 204.74 in the downstream slices, where the cross-sectional area decreases along the main flow direction (see sketch at left).

Length of the left arrow represents the magnitude of the main flow velocity v_z at the pore center ($x = y = z = 0$) of 8.66 and 29.78 mm/s for $Re = 59.78$ and 204.74, respectively.

originate from the plane $z = -1$, and the two outside ones originate from the plane $z = 0$. The streamlines are represented by the path of fluid particles in constant time intervals, and the tangential location of the particle is represented by the color scale. The three centermost particles flow along the surface of the bottom sphere, approach the top sphere, and then turn along the surface. The outer two particles move slowly downward and then move toward the pore center before moving downstream. Strong sheer stress between the jet-like flow at the center of the pore and near stagnant flow between the spheres results in circulations about the main flow direction. The circulation can also be explained by the interaction, which turns the flow towards the stagnant spaces, of the jet-like flow with the sphere surface as shown in the eddies of slice A in Figure 10b. In other words, flow away from the central jet strikes the sphere, and then turns towards the stagnant regions thus resulting in a circular flow in the *x-y* plane.

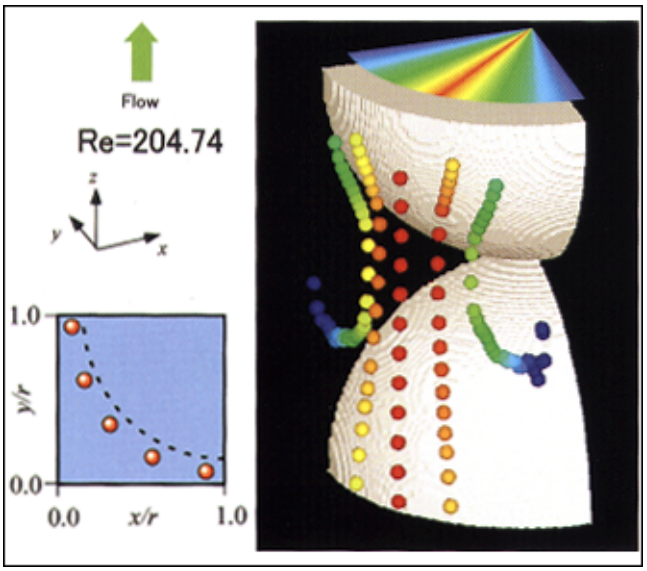

Figure 11. Streamlines in the pore at *Re* = 204.74.

Five streamlines are represented by the trace of fluid particles at constant time intervals. Initial points of the particles are shown in the *x-y* plane on the left. The three centermost particles originated from $z = -1$, the outer two started at $z = 0$. Flow direction is from bottom to top and the tangential position is represented by the color scale at top.

Conclusions

We used an MRI technique to directly measure the velocity distributions of inertial flow in a pore space that models a simply packed bed. The 3-D flow field was imaged at Reynolds numbers of 12.17, 59.78, and 204.74, whereas the *z*-component of flow was also determined at $z = 0$ with $Re = 28.88$ and 105.57.

At $Re = 12.17$, the fluid speed decreased with increasing cross-sectional area and increased with decreasing cross-sectional area like a creeping flow; in this regime, the local geometry significantly influenced the flow. The transition from creeping flow to inertial flow was not clearly observed.

However, at $Re = 59.78$, unlike the case at lower *Re*, the velocity along the flow direction did not simply decrease with an increasing cross-sectional area and did not simply increase with decreasing cross-sectional area further downstream. Instead, the flow speed had a minimum that was downstream from the maximum in the cross-sectional area. This is attributed to the increasing role of inertial forces over viscous forces as the Reynolds number increases.

Inertial forces were even more dominant at $Re = 204.74$; in this case, the fluid flowed through the pores like a jet without changing velocity. The maximum velocity in the center of the pore increased with increasing Reynolds number by a factor of up to four times as high as the pore-averaged velocity; this factor of four was reached for a Reynolds number from 59.78 to 204.74.

The interaction between jet-like flow through the center and the spherical surfaces resulted in some backflow near the bounding surfaces with magnitudes of up to 0.5 times the mean pore velocity. The location of this backflow changed significantly with position along the main flow and with the Reynolds number. Extensive backflow occurred near the spheres' surfaces where the flow cross-sectional area increased along the main flow direction. In addition, the jet-like flow collided with the surfaces where the cross-sectional area decreased, and then turned towards the stagnant spaces. The circulation in the stagnant spaces can be explained by the strong sheer stress between the jet-like flow and stagnant flow, as well as by the interaction of the jet-like flow with the spheres. This turning of the flow generated eight symmetrical eddies in the plane perpendicular to the main flow direction.

Within the simply packed bed of this study, the velocity profile is parabolic even for a high local Reynolds number because the jet-like flow penetrates through the center of the pores without changing direction. This implies that the dependence of the variance of the velocity distribution on the local Reynolds number is different from that of a randomly packed bed.

Acknowledgments

The authors thank N. Iwatsuki for technical advice on manufacturing the unit cells by using the high-speed prototyping system and K. Ogawa, who helped with the MRI.

Literature Cited

Baumann, T., R. Petsch, and R. Niessner, "Direct 3-D Measurement of the Flow Velocity in Porous Media Using Magnetic Resonance Tomography," *Environ. Sci. Technol.*, **34**, 4242 (2000).

Bear, J., *Dynamics of Fluids in Porous Media*, Dover Publications, New York (1972).

Bories, S. A., M. C. Charrier-Mojtabi, D. Houi, and P. G. Raynaud, "Non Invasive Measurement Techniques in Porous Media," *Convective Heat and Mass Transfer in Porous Media*, S. Kakac et al., eds., Kluwer Academic Publishers, Netherlands, p. 883 (1991).

Callaghan, P. T., *Principles of Nuclear Magnetic Resonance Microscopy*, Clarendon Press, Oxford (1991).

Dybbs, A., and R. V. Edwards, "A New Look at Porous Media Fluid Mechanics—Darcy to Tubulent," *Fundamentals of Transport Phenomena in Porous Media*, Bear and Corapcioglu, eds., Martinus Nijhoff Publishers, Boston, p. 201 (1984).

Feinauer, A., S. A. Altobelli, and E. Fukushima, "NMR Measurements of Flow Profiles in a Coarse Bed of Packed Spheres," *Magn. Resonance Imaging*, **15**, 479 (1997).

Fukushima, E., "Nuclear Magnetic Resonance as a Tool to Study Flow," *Annu. Rev. Fluid Mech.*, **31**, 95 (1999).

Irwin, N. C., R. A. Greenkorn, S. A. Altobelli, and J. H. Cushman, "Examination of Stochastic Dispersion Theory by MRI in Aperiodic Porous Media," *AIChE J.*, **46**, 2345 (2000).

Johns, M. L., A. J. Sederman, A. S. Bramley, and L. F. Gladden, "Local Transitions in Flow Phenomena through Packed Beds Identified by MRI," *AIChE J.*, **46**, 2151 (2000).

Jolls, K. R., and T. J. Hanratty, "Transition to Turbulence for Flow through a Dumped Bed of Spheres," *Chem. Eng. Sci.*, **21**, 1185 (1966).

Kaviany, M., *Principles of Heat Transfer in Porous Media*, 2nd ed., Springer-Verlag, New York (1995).

Kutsovsky, Y. E., L. E. Scriven, H. T. Davis, and B. E. Hammer, "NMR Imaging of Velocity Profiles and Velocity Distributions in Bead Packs," *Phys. Fluids*, **8**, 863 (1996).

Li, T. Q., J. D. Seymour, R. L. Powell, M. J. McCarthy, K. L. McCarthy, and L. Ödberg, "Visualization of Flow Patterns of Cellulose Fiber Suspensions by NMR Imaging," *AIChE J.*, **40**, 1409 (1994).

Manz, B., L. F. Gladden, and P. B. Warren, "Flow and Dispersion in Porous Media: Lattice-Boltzmann and NMR Studies," *AIChE J.*, **45**, 1845 (1999).

Montemagno, C. D., and W. G. Gray, "Photoluminescent Volumetric Imaging: A Technique for the Exploration of Multiphase Flow and Transport in Porous Media," *Geophys. Res. Lett.*, **22**, 425 (1995).

Moroni, M., and J. H. Cushman, "Statistical Mechanics with Three-Dimensional Particle Tracking Velocimetry Experiments in the Study of Anomalous Dispersion. II. Experiments," *Phys. Fluid*, **13**, 81 (2001).

Ogawa, K., Y. Yokouchi, and S. Hirai, "Correlation between Interstitial Flow and Pore Structure in Packed Bed (1st. Report, Axial Velocity Measurement Using MRI and Visualization of Axial Channel Flow) (in Japanese)," *Trans. Japan Soc. Mech. Eng.*, **66B**, 131 (2000).

Rashidi, M., A. Tompson, T. Kulp, and L. Peurrung, "3-D Microscopic Measurement and Analysis of Chemical Flow and Transport in Porous Media," *J. Fluid Eng.-Trans. Amer. Soc. Mech. Eng.*, **118**, 470 (1996).

Saleh, S., J. F. Thovert, and P. M. Adler, "Flow along Porous Media by Particle Image Velocimetry," *AIChE J.*, **39**, 1765 (1993).

Sederman, A. J., M. L. Johns, A. S. Bramley, P. Alexander, and L. F. Gladden, "Magnetic Resonance Imaging of Liquid Flow and Pore Structure within Packed Beds," *Chem. Eng. Sci.*, **52**, 2239 (1997).

Sederman, A. J., M. L. Johns, P. Alexander, and L. F. Gladden, "Structure-Flow Correlations in Packed Beds," *Chem. Eng. Sci.,* **53**, 2117 (1998).

Seymour, J. D., and P. T. Callaghan, "Generalized Approach to NMR Analysis of Flow and Dispersion in Porous Media," *AIChE J.*, **43**, 2096 (1997).

Shattuck, M., R. Behringer, J. Geordiadis, and G. A. Johnson, "Magnetic Resonance Imaging of Interstitial Velocity Distributions in Porous Media," *Proc. of ASME/FED on Experimental Techniques in Multiphase Flows*, **125**, 39 (1991).

Shattuck, M. D., R. P. Behringer, G. A. Johnson, and J. G. Georgiadis, "Onset and Stability of Convection in Porous Media: Visualization by Magnetic Resonance Imaging," *Phys. Rev. Lett.*, **75**, 1934 (1995).

Stephenson, J. L., and W. E. Stewart, "Optical Measurements of Porosity and Fluid Motion in Packed Bed," *Chem. Eng. Sci.*, **41**, 2161 (1986).

Yevseyev, A. R., V. E. Nakoryakov, and N. N. Romanov, "Experimental Investigation of a Turbulent Filtrational Flow," *Int. J. Multiphase Flow*, **17**, 103 (1991).

Manuscript received Nov. 27, 2001, and revision received May 28, 2002.